ADVANCED FUNCTIONAL MATERIALS
www.afm-journal.de

Full 3D Printing of Stretchable Piezoresistive Sensor with Hierarchical Porosity and Multimodulus Architecture

*Ziya Wang, Xiao Guan, Huayi Huang, Haifei Wang, Waner Lin, and Zhengchun Peng**

A soft piezoresistive sensor with its unique characteristics, such as human skin, light weight, and multiple functions, yields a variety of possible practical applications to skin-attachable electronics, human–machine interfaces, and electronic skins. However, conventional filler-matrix piezoresistive sensors often suffer from unsatisfactory sensitivity or insufficient measurement range, as well as significant cross-correlation between out-of-plane pressure and in-plane extension. Here, a stretchable piezoresistive sensor (SPS) is realized by combining a hierarchically porous sensing element with a multimodulus device architecture via a full 3D printing process. As a result, the sensor exhibits high sensitivity (5.54 kPa^{-1}), large measurement range (from 10 Pa to 800 kPa), limited cross-correlation, and excellent durability. Meanwhile, benefiting from the porous structure and mechanical mismatch design, which efficiently distributes the stress away from the sensing element, the device experiences only 7% resistance change at 50% stretching. This approach is employed to rapidly program and readily manufacture stylish, all-in-one, functional devices for various applications, demonstrating that the technique is promising for customized stretchable electronics.

1. Introduction

Advances in soft electronics are enabling the fast development of smart fields for personalized health-monitoring,[1] human–machine interfaces,[2] electronic skin,[3] soft robotics,[4] and so forth. The burgeoning market demand soft electronics including perceptive devices to provide new sources of advantage. For instance, piezoresistive pressure sensors underscore their inherent flexibility/stretchability, low energy consumption, easy read-out, broad range of pressure detection, facile, and scalable fabrication processes.[5,6] However, for most piezoresistive sensors, the active layer is a planar elastomer composite incorporated with conductive materials (reduced graphene oxide, carbon nanotubes, metal particles, etc.).[7–9] This design often suffers from either unsatisfactory sensitivity or insufficient detection range, because the pressure response region is restricted by the percolation threshold.[10,11] Although many works were reported adopting more sensitive nanomaterials or complicated microstructures (e.g., interlocked microstructure) to improve sensitivity,[12,13] the research community has yet limited understanding on the intrinsic structure–property relationship of perceptive devices. Reasonable filler distribution and interspace structure design are still a critical challenge, particularly for a stretchable multimaterial system.[14] Moreover, costly ingredients and fabrication processes deterred the scalable production and application of soft electronics.[15–17]

Herein, we demonstrated a stretchable piezoresistive sensor (SPS) fabricated by a low-cost and easily accessible template method. The NaCl particles were first premixed in a polymer ink for a printable hierarchically porous architecture. The synergy between subtle carbon black (CB) conductive network with excessive porous structure and hierarchical porosity design substantially enhance the sensitivity and measurement range of the sensor, respectively. Yet traditionally, difficulties and complexities in controlling pore characteristics for an integrated all-in-one device still remain.[18] Therefore, by taking advantage of the rheological properties of polymer matrix, we develop a ink writing technique to pattern the multifarious soft materials with high-dimensional geometries (3D printing).[19–21] The fully 3D-printed SPS is composed of an elastomer substrate, a pair of double helix interdigital electrodes (electrode layer) and a highly resilient piezoresistive sensing element (sensing layer) (**Figure 1**a). Each layer can be customized with tunable mechanical and electrical properties and edited into any shape and size according to the application scenarios.[22,23] In previous studies, the out-of-plane pressure and the in-plane extension of soft pressure sensor are usually difficult to be distinguished due to identical resistance-change mechanism. We adopted a multilayered and multimodulus strategy in the 3D printing processes to restrain the device response to in-plane extension. Unlike the conventional predesigned strategies of stretchable electronics typically employing serpentine and buckled structures,[24,25] our architecture can concentrate stress to the interdigital electrodes and substrate underneath the piezoresistive sensing element, as verified by the following finite element analysis (FEA).

Dr. Z. Wang, X. Guan, H. Huang, Dr. H. Wang, W. Lin, Prof. Z. Peng
Center for Stretchable Electronics and Nano Sensors
Key Laboratory of Optoelectronic Devices and Systems of Ministry of Education
College of Optoelectronic Engineering
Shenzhen University
Shenzhen 518060, P. R. China
E-mail: zcpeng@szu.edu.cn

The ORCID identification number(s) for the author(s) of this article can be found under https://doi.org/10.1002/adfm.201807569.

DOI: 10.1002/adfm.201807569

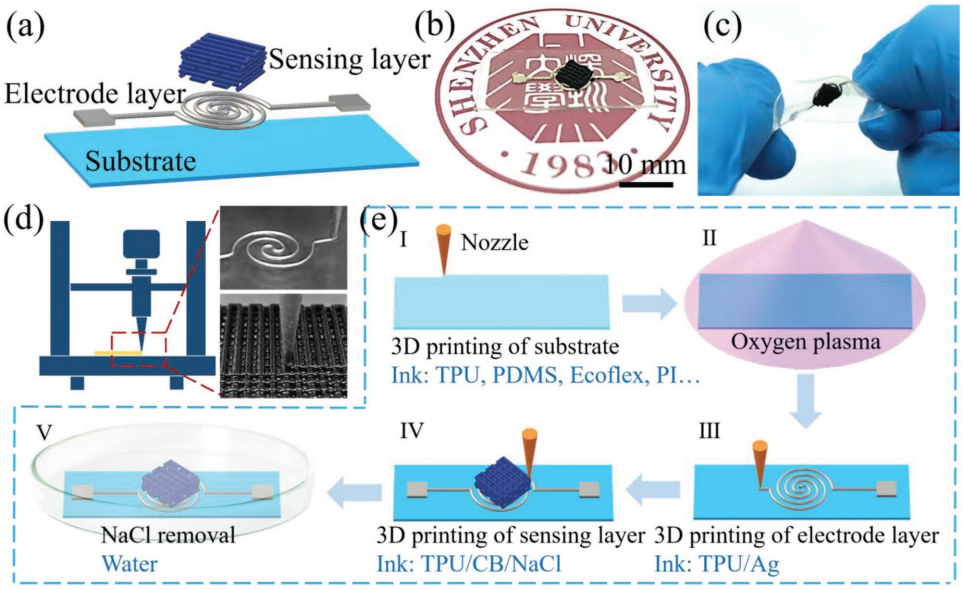

Figure 1. The design and technological flow chart of SPS. a) Schematic structure of the SPS device. Optical image of a representative SPS under b) natural and c) twisting states. d) Schematic illustration of direct ink writing (DIW) 3D printer and images of monolayer (electrode layer ink) and multilayer (sensing layer ink) structure printing processes. e) 3D printed step-by-step diagram, including 3D printing of each layers, surface treatment and removing NaCl template.

2. Results and Discussion

A fabricated SPS and the schematics of the 3D printing processes are shown in Figure 1. Figure 1b,c shows the optical images of a representative SPS at relaxed and 360° twisted states, respectively, revealing excellent softness as well as mechanical robustness of the sensor. The fabrication of SPS by 3D printing process is illustrated in Figure 1d,e and Movie S1 (Supporting Information). Figure S3 (Supporting Information) provides the viscoelastic characters of the printing inks for three layers of the SPS. With strong shear thinning behavior and large storage modulus, the filaments can be continuously and uniformly ejected from the fine nozzle and stacked layer-by-layer to build the designed 3D structure. The sensing area of the representative device is 6×6 mm. Nevertheless, 3D printing can realize SPS with any customized shape and size in order to meet the demands of all kinds of applications (Figure S4, Supporting Information).

To develop an optimal ink for the electrode layer, we mixed silver microflakes (≈5 µm lateral dimension) within a thermoplastic urethane elastomer (TPU, micromorphology described in Figure S5, Supporting Information). The stress–strain behavior of the TPU/Ag conductive ink as a function of Ag loading is displayed in Figure S6a (Supporting Information). Apparently, higher Ag content leads to reduced stretchability and increased modulus. As such, TPU/90% Ag shows the inferior stretching capacity (fractured at 27% strain) because of too low relative content of polymer adhesive. On the other hand, the electrical conductivity of the TPU/Ag composites follows the power-law theory of percolating network.[26] The resistance exponentially decreases with the increase of Ag loading, and the percolation threshold is found to be 65 wt% of Ag (Figure S6b, Supporting Information). **Figure 2**a summaries the resistance changes of TPU/Ag with varied Ag content during a continuous in situ stretching. All samples experience a linear, minor resistance increase under stretching, until the percolation node is reached and an exponential increase occurs. The analysis found that higher Ag concentration can effectively shift the percolation node toward higher value, ensuring better stability of electrode conductivity under stretching. Taking together, TPU/85% Ag, which synergistically possesses excellent mechanical property (more than 120% of tensile elongation), very low stretching resistance compared with other components of the sensor (less than 0.7 Ω resistance change at 50% tensile, Figure S6c, Supporting Information) and negligible compression resistance change (less than 0.05 Ω resistance change under pressure of 600 kPa, Figure S6d, Supporting Information), is considered as the appropriate electrode layer ink.

For the sensing layer, we employ a sacrificial NaCl template, highly conductive CB nanoparticles and soluble TPU as precursors. Interestingly, once controlling the size of NaCl particles (<100 µm), these solids can be held together in a thixotropic granular paste by capillary attraction.[27] This granular paste greatly facilitates the filament stacking, without affecting the direct ink writing processes. The electronic and mechanical characteristics of the sensing layer with different formulation were systematically studied. Figure 2b demonstrates that stretching resistance of sensing layer is more stable with increasing content of NaCl (at the same CB weight ratio of 20%). Larger number of homogeneous apertures produced by the NaCl template absorb partial stretching strain. The change becomes small after the mixing ratio exceeds 400%. The stretching resistance has the same tendency with respect to the increase of CB content at a fixed NaCl content (Figure 2c). However, the excessive NaCl and CB contents lead to easy fracture of the elastomer. For instance, the sensing layers with 25% CB was broken at strain as low as 53%. Figure S7 (Supporting Information) compares the resistances and fracture strains of

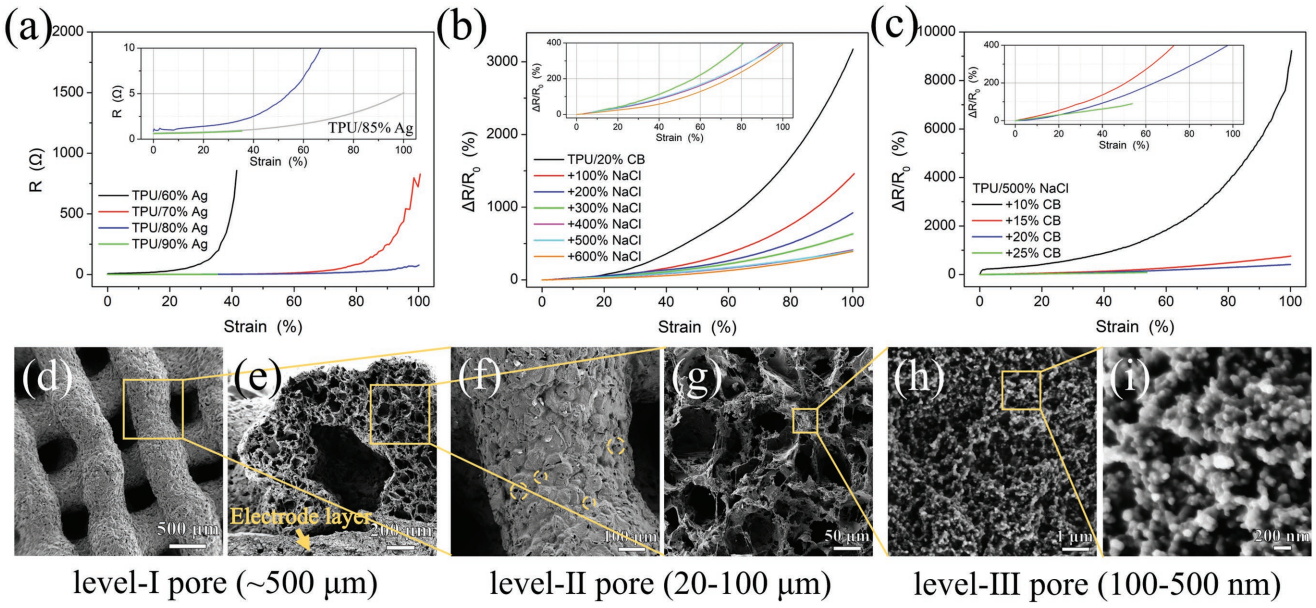

Figure 2. Stretching behavior of inks and hierarchically porous architecture. a) Resistance as a function of applied stretching for electrode layer inks. Plot of $\Delta R/R_0$ versus strain varying b) NaCl and c) CB contents of sensing layer inks. d–i) SEM images of hierarchically porous 3D printed sensing layer at various scales.

sensing layers composed of different NaCl and CB contents, as well as the resistance change of the planar samples under compression. As a result, we deliberate that an ink containing 500% NaCl and 20% CB is the optimum choice for the sensing layer.

The microstructure and porosity of printed sensing layer were characterized via scanning electron microscopy (SEM, Figure 2d–i; Figure S8, Supporting Information). A representative sensing layer consists of six layers of zigzag filaments stacked on top of each other, forming a multilayered mesh structure. The top view (Figure 2d) shows that the open mesh configuration is macroporous (level-I pore, ≈0.5 mm), comprised of ≈0.5 mm wide filaments. On the surface of the filaments (Figure 2f), we observed the void holes with size about several microns, left behind when NaCl fillers were dissolved. The cross-sectional SEM images of the filaments in Figure 2e,g show the NaCl template-induced microscale pores (level-II pore, 20–100 μm). Plenty of exposed CB nanoparticles were found across the surface of pore walls, helping with improving the device sensitivity. The densely packed CB nanoparticles around the voids were bonded by TPU, building a monolithic sensing layer elastomer with an intrinsic pore size of 100–500 nm (level-III pores) (Figure 2h,i). With the homogeneous hierarchically porous microstructure, there will be an increased area of contact among conductive walls under pressure loading, resulting in a decrease of both the contact resistance and channel resistance.[28] Meanwhile, CB nanoparticles are forced to pack more closely, enhancing the electrical conduction pathways.

The mechanoelectrical response of SPS was studied to investigate the effect of the number of stacked sensing layers. Figure S9a (Supporting Information) shows the measurement of the thickness of sensing elements. The printed devices demonstrate a good linear relationship with average thickness ≈180 μm per layer, benefiting from the steady rheological property of the ink. Figure S9b (Supporting Information) describes the typical resistance change curves of 1–8 layers of SPS with respect to the loading pressure. As expected, the sensitivity and resistance change rate increase with the increasing number of stacked layers (**Figure 3**a). However, the trending slows down after the sensing element is comprised of more than 6 stacking layers. Therefore, a 6-layer-SPS would be an optimal choice for most applications.

Compared to the planarly structured sensing layer, the 3D printed SPS exhibits a higher sensitivity across a wide measurement range. The typical resistance response curve of 6-layered SPS is composed of three linear regions (Figure 3b). The fitted sensitivities are 5.54 kPa^{-1} for the low-pressure range (<10 kPa), 0.123 kPa^{-1} for the middle-pressure range (10–100 kPa) and 0.0048 kPa^{-1} for the high-pressure range (100–800 kPa), respectively. Under a low-pressure loading, the microscale elastic deformation can easily close the nanopores (level-III pores) stationed into the agglomerated CB nanoparticles, dropping the resistance of the sensing layer. Further increase of applied pressure starts to close level-II pores and continues to drop the resistance of the sensing layer. As pressure loading keeps increasing, severe flattening of 3D printed filaments occurs, causing the level-I pores to close and the resistance of the sensing layer drop even more. As a key figure of merit to evaluate sensor performance, the gauge factor of the SPS was calculated to be 13.3, which is comparable to many other particle-laden composites based strain sensors.[29–31] In addition, the intrinsic resistance of our device is less than 100 Ω, significantly smaller than other piezoresistive sensors reported so far, leading to remarkable reduction of the power consumption due to Joule heating. In a word, the high sensitivity, large measurement range and low energy consumption demonstrate significant improvements in comparison with recent studies, summarized in Table S2 (Supporting Information). Especially, our approach to realizing high sensitivity and large measurement range by hierarchical

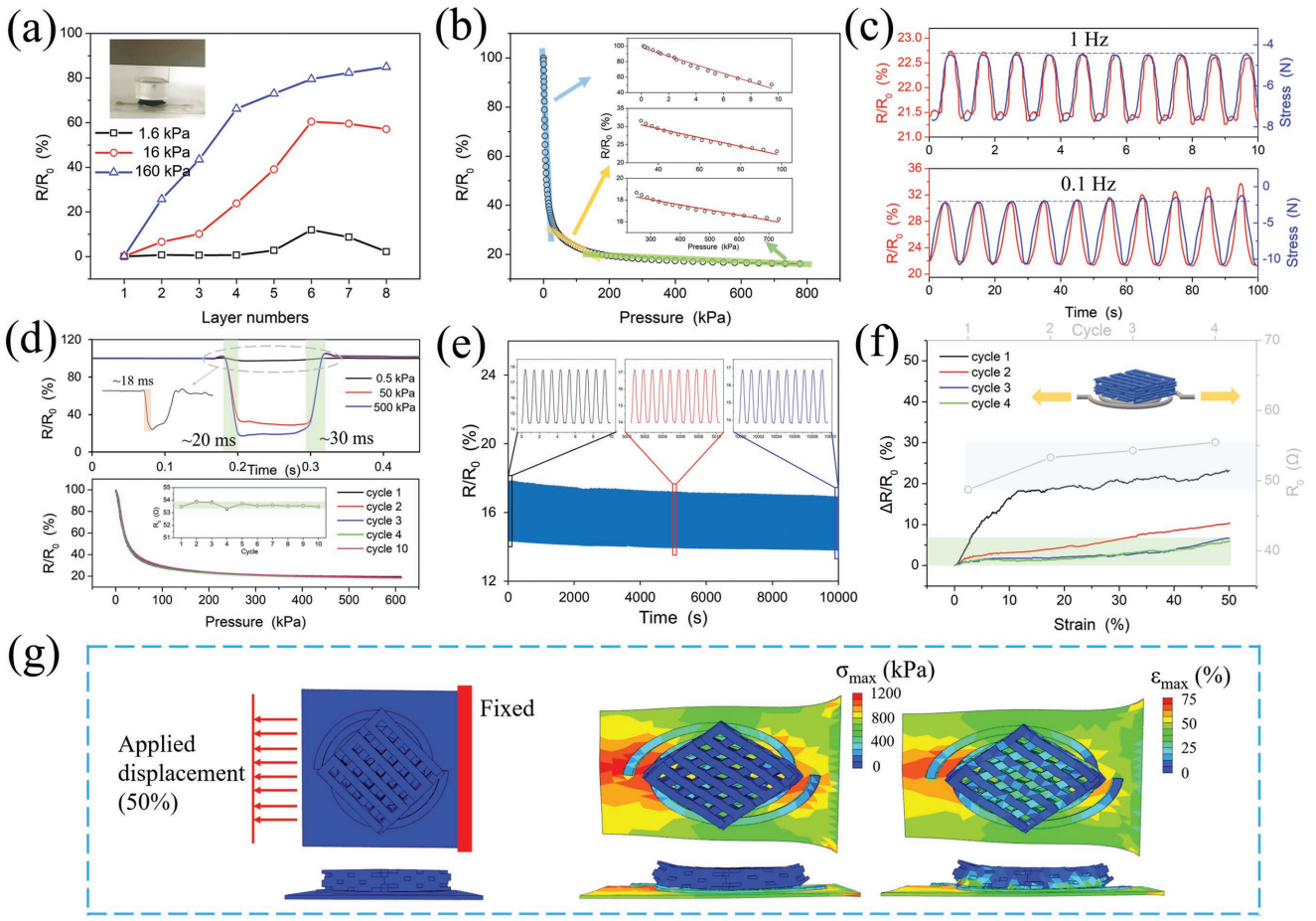

Figure 3. Evaluation of electromechanical performances of SPS. a) Relative resistance changes as a function of layer numbers of SPS at different pressure loadings. b) Resistance response of 6-layer SPS versus pressure loading. c) The dynamic responses of the 6-layer SPS at different pressures and frequencies. d) The response time and the repeatability of SPS at a large measurement window. e) Stability and durability test of SPS over 10 000 loading-unloading cycles at a frequency of 1 Hz. f) Relative resistance and initial resistance changes of the SPS obtained from stretching cycles. g) Contour plots of the strain and stress distributions in the SPS under 50% stretched status by FEM study.

porosity design is very simple, superior to the design of pressure sensor using dual-mode sensing elements.[32]

To investigate the dynamic response of the SPS, sinusoidal pressure cycles with two different frequencies were employed (Figure 3c). Observably, the SPS always responds synchronously and repeatedly during both tests. The response times and releasing times were found to be ≈20 and ≈30 ms, respectively, under various applied pressure (Figure 3d (top)). Densely packed CB particles with nanosized pores effectively make short the bridging time of conductive access. Figure 3d (bottom) confirms the high repeatability in relative resistance change among different pressure cycles with large measurement range. The durability of SPS was measured by a repetitive contact test (40–200 kPa) for more than 10 000 cycles at a frequency of 1 Hz (Figure 3e). Despite a slight drift, the SPS exhibits stable and reproducible performance without functional degeneration. And the microstructure characterizations of Figure S10 (Supporting Information) proves that SPS maintains the structural integrity after experiencing long-term compression cycling.

The elasticity of the SPS was explored up to 50% strain, which is well beyond the stretchability of human skin (≈30%). Identical polymer matrix in interface prevents the delamination problem. The electrical performance under iterative stretching test (Figure 3f) shows the freshly made SPS can achieve repeatable pressure readings after the first two cycles. Remarkably, the normalized change in resistance ($\Delta R/R_0$) of SPS was kept below 7% up to 50% strain. Meanwhile, the FEA results (Figure 3g) reveal that the maximum stress in the sensing layer is only about 5% when the SPS is stretched up to 50% strain, consistent with the test results. The excellent in-plane stability guarantees an accurate determination of out-of-plane pressure of soft piezoresistive sensor. The performances of our SPS device are largely superior to recently reported stretchable pressure sensors with differentiated conductive materials and structural configurations.[17]

The great electromechanical stability of our SPS can be attributed to the unique multimodulus design of the multilayered device and the hierarchically porous structure of the sensing layer. First, there are apparent differences in ductility and mechanical mismatch among the three layers of the SPS (Figure S11d, Supporting Information). The elastic modulus of the electrode layer (2.96 MPa) is much larger than that of the

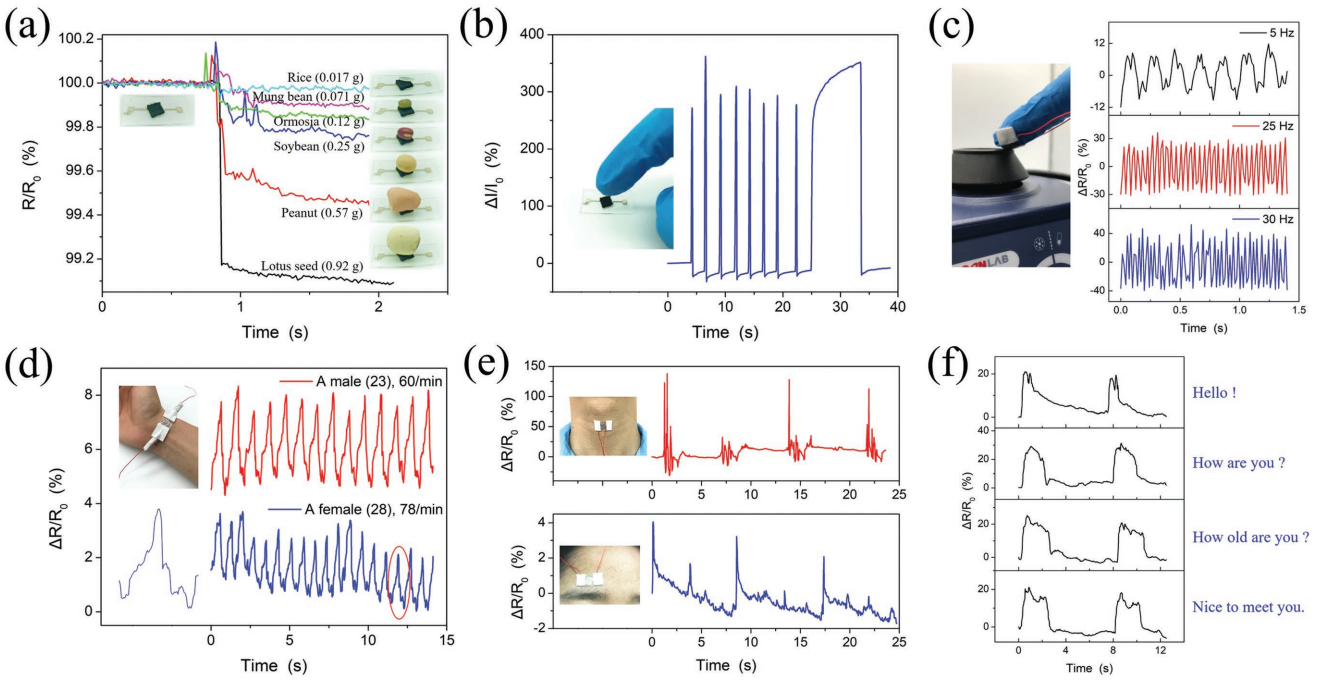

Figure 4. Applications of the 3D printed SPS. a) Weighing common grains. b) Tracking the tapping motions of a finger. c) Measuring the dynamic vibration of a machine. d) Monitoring pulse by simply laying a SPS on the wrist without signal processing. e) Monitoring the swallowing and blinking motions. f) Monitoring muscle motions during speech.

substrate (0.98 MPa) as well as the sensing layer (0.38 MPa). With this mechanical mismatch between electrode layer and the substrate, under stretching the stress is largely distributed onto the substrate, because the electrode layer is much stiffer. Therefore, the electromechanical stability of electrode is protected to some extent. This is similar to the "island-bridge" model. In addition, the double helix design of the electrode pair helps further reduce the impact on the electromechanical stability from stretching. Second, with multiple levels of network in the sensing layer, the bottom level network, which intermediately attaches to the electrodes and the substrate, absorbs more stress than the level above, minimizing the strain experienced by the upper levels of network in the sensing layer. From the cross-sectional results of FEA (Figure 3g), this strategy was found to be very effective, resulting in an overall stable sensing element when the device is subjected to stretching. The low elastic modulus of the sensing element also augments the deformability of the sensing layer under the action of an applied pressure. Third, not only does the porosity of the sensing layer facilitate the absorption of the stretching stress, but the closing of the pores during stretching also helps reduce the electrical resistance of the sensing layer. For comparison purposes, a solid blocky sensing layer was made, which shows a 30% more resistance change under the same conditions (Figure S11a, Supporting Information). Besides, the nanoparticulate conductors can absorb partial disturbances and improve the signal-to-noise ratio. As a result, the stretchable SPS presents diversified application scenarios, for example, skin-mountable monitoring on highly deformable palms.

Common grains were employed to evaluate the static pressure detection limit of SPS to embody the high sensitivity. The object as light as a grain of rice (≈10 Pa) and a mung bean (≈23 Pa) can be detected through a measurable resistance response, as presented in **Figure 4**a. Figure 4b shows the SPS's transient and steady state force responses to the repeated finger taps. The $\Delta R/R_0$ were found to be over 300% easily. Even better, the sensor with its adaptability can reliably operate under the water (Figure S12a, Supporting Information). As a demonstration of the capability to measure the dynamic pressures from limb tremor to machine vibration, SPS was glued to the fingertip and to touch an experimental mixer. The signal responses to simulated vibrations were expressed precisely at frequency of 5 Hz (Parkinson's disease), 25 and 30 Hz, respectively, approving the rapid response and excellent reproducibility of SPS (Figure 4c). Moreover, SPS is also an efficient ion concentration and humidity sensor simultaneously, which carries forward the all-in-one concept of electronic skin. The section involved physical mechanisms and related applications are discussed in Figure S12b–d (Supporting Information).

Next, the versatile SPS was put on the artery of a wrist for real-time monitoring of pulse beats (Figure 4d and Movie S2, Supporting Information). Thanks to the superior sensitivity and signal-to-noise ratio, representative radial artery pressure waveforms without any signal amplification and postprocessing clearly indicate three wave components: percussion wave, tidal wave and diastolic wave (P_1, P_2, and P_3). As common parameters for diagnosis of arterial stiffness, the calculated radial artery augmentation index ($AI_r = P_2/P_1$) and radial diastolic augmentation index ($DAI = P_3/P_1$) are 0.50 and 0.23 on average, respectively, for a 28-year-old female, showing good agreements with reference values.[33,34] Interestingly, SPS can also provide a basic pulse signal that can induce ballistocardiogram (BCG)

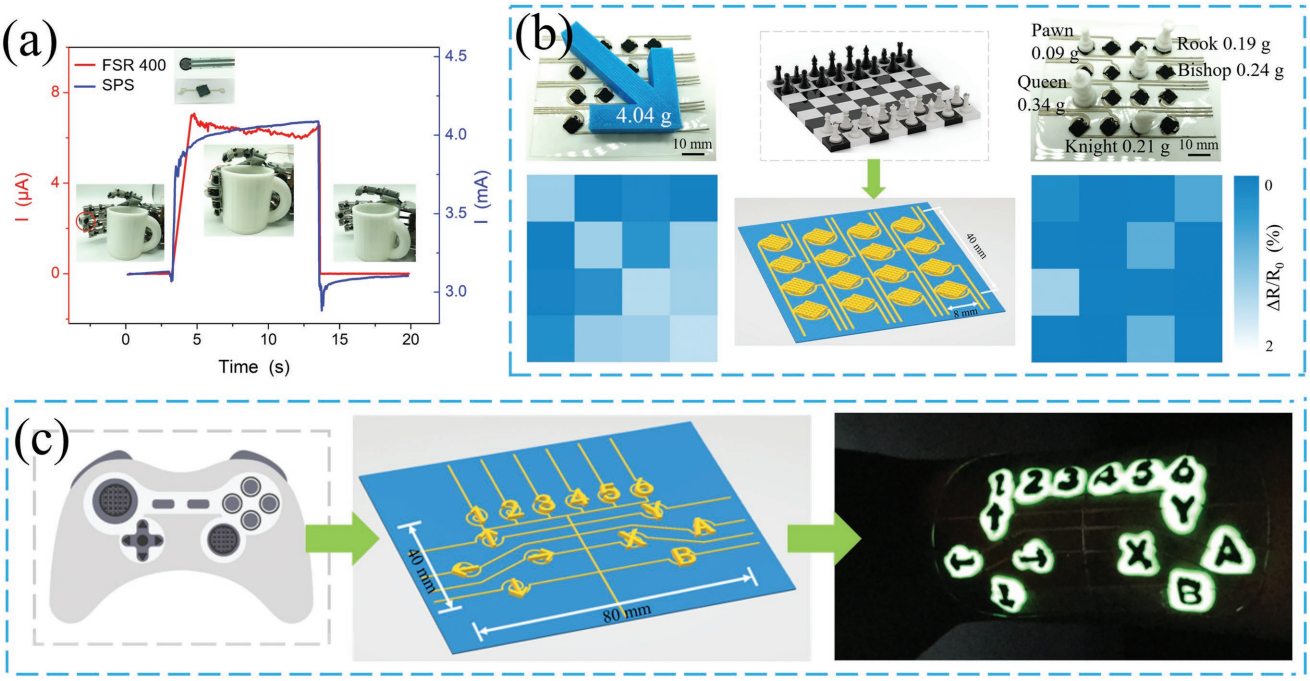

Figure 5. Customization of SPS arrays for various applications. a) Monitoring a robotic hand grabbing and transferring a cup. b) Signal mapping of the pressure distribution for an arrow-shaped object and mini chesses on the surface of the 4 × 4 pixel SPS, respectively. c) A 3D-printed thin and stretchable gamepad.

with characteristic signs of H, I, J, K, and L by applying slight pressure (Figure S13a, Supporting Information). BCG, which cannot be collected by traditional electrocardiogram (ECG) monitor, is a measure of the body's mechanical reaction to the blood ejected during systole.[35] That is, SPS has adequate capacity to capture the multifarious biological signals for convenient personal healthcare, even the finger-tip pulse (described in Figure S13b of the Supporting Information). In addition, SPS can accurately express the messages that are generated from the weak muscle movement of human body, such as swallowing (Figure 4e (top)), blinking (Figure 4e (bottom)), phonation (Figure 4f), and breathing (Figure S12d, Supporting Information), thus developing into the wide potential applications in emotion monitoring and vitro diagnostics. Typically, the sensor shows the characteristic resistance patterns when speaker pronounces the different words and phrases, like "Hello," "How are you," and "How old are you." This reproducible sensing of phonation recognition is likely to be an effective auxiliary tool for deaf people speaking.

To demonstrate the mutual sensing capability of touching and grasping, a SPS and a similar-sized commercial flexible pressure sensor (FSR 400) were adhered to the fingers of a programmable humanoid robot hand. When the robot hand executes the task of holding and transferring a cup, the SPS exhibits a faster force response, a more rapid signal feedback than commercial sensor (**Figure 5**a). 3D Printing is advantaged in the convenience and operability. We readily scaled up the sensor layouts to an array configuration with required pixels to collect the spatial pressure information. As a demonstration, when an arrow-shaped polylactic acid plate was placed on the sensor arrays, the output signal intensity of a fully printed 4 × 4 pixel array can literally represent the object silhouette and the color contrast mapped local pressure distributions (Figure 5b). Positions information of objects also can be monitored. Every different mini chesses are marked on the chrominance mapping of the SPS array. These data can be fed to a computer for tracking and analysis, just as a smart chess board.

The versatility and customizability in 3D style of editable tactile sensors promise a wide range of applications in wearable and portable electronics. We designed a customized soft gamepad composed of 16 SPS keypads. A noctilucent powder-doped poly(dimethylsiloxane) (PDMS) is used as the extra border to enhance the night visualization. Figure 5c displays the fully 3D-printed soft gamepad can be conformally attached onto the human wrist. Various scenarios, such as PC games, remote controllers and assistive communication devices can easily be implemented with the SPS gamepad. For example, we present a demo of Super Mario Bros. (Movie S3, Supporting Information). All kinds of orders would be executed when the distinct SPSs got in touch, including omnidirectional running, jumping, attacking, and even the travelling speed of roles which can also be controlled by the pressure level.

3. Conclusion

In conclusion, we designed a hierarchically porous sensing architecture to enhance both the sensitivity and measurement range of a stretchable piezoresistive sensor. Carbon black nanoparticles and sacrificial NaCl template were evenly dispersed into TPU elastomer matrix, forming a printable ink to fully 3D-print the sensor and sensor array. The novel multilayered

and multimodulus strategy achieved stable out-of-plane pressure response and minimized in-plane stretching disturbance. This work also demonstrates the fabrication of functional devices by directly writing as a generalized and customizable approach for stretchable sensors. The results reveal the significance of combining the structural engineering of sensing materials with device design to realize advanced soft electronics for a great many valuable applications, such as health monitoring, robotics tactile sensing, and human–machine interfaces.

4. Experimental Section

Preparation of Printing Inks: The base and curing agent of PDMS (Sylgard 184, Dow Corning) were mixed together at weight ratio of 10:1, degassed, and used as substrate ink directly. The electrode layer ink was prepared by dissolving TPU (Elastollan 35A, BASF) in *N*,*N*-dimethylformamide (DMF) solvent in 1:1.5 weight ratio (TPU:DMF). Following, silver microflakes (≈5 µm, 99.99%, HONGWU New Materials) were added into the dissolved TPU and homogenized using a planetary mixer for 30 min. The sensing layer ink was compounded by employing NaCl crystals as the sacrificial template. First, the grain sizes of NaCl particulates were reduced by planetary ball milling (F-P400, FOCUCY) at a speed of 540 rpm for 20 min. Then a certain ratio of NaCl (sizes <100 µm), CB (SUPER P Li, TIMCAL) and TPU (dissolved in twice its weight of DMF) were mixed thoroughly to obtain this porous and conductive printable ink. All chemicals were used as received without purification. To exclusively measure mechanical and electronic performances of above inks, the conventional planar structures (5 × 10 mm) were prepared by coating these viscous polymer composites between two glass substrates with a 1.2 mm gap, respectively.

3D Printing: The SPS was fabricated by a custom-built 3D printer (Figure S1, Supporting Information). All printing paths were determined using G-code commands, which were generated by commercial software (Ultimaker Cura) from designed 3D models. Printed PDMS substrate with a thickness of about 200 µm (840 µm nozzle) was cured at 80 °C for 2 h and then treated in oxygen plasma for 2 min (100 W, Tergeo, PIE). The electrode layer and sensing layer inks were housed in separate syringes (10 mL barrel) with a disposable tapered nozzle of 260 and 410 µm inner diameters, respectively. A precise stepper motor provides the programming pressure for extruding the high-viscosity ink. The usual printing speed is 20 mm s^{-1}, accordingly, the single SPS can be printed within 1 min. After printing, the SPSs were dried at 110 °C in an oven for 6 h and subsequently were overall immersed in water which was replaced several times to completely removed NaCl for two days. The 4 × 4 pixel array has a common stretchable substrate, common-grounded electrode layers and 16 separated sensing layers for temporal and spatial resolved, patterned pressure sensor array.

Characterization: The morphologies and microstructures of the samples were observed by field-emission scanning electron microscope (FESEM, Supra 55 Sapphire, ZEISS). The sheet resistance was measured by a four-point probe method on a Keithley 2400 source meter. The rheological behaviors of printing inks were characterized using a controlled stress rheometer (AR1000, TA Instruments) under ambient conditions. Shear storage modulus (G') and viscous loss modulus (G'') were measured in an oscillatory mode.

Electromechanical Measurements: Planar solidified ink and SPSs were mounted on a uniaxial tensile and compression testing instrument (E1000, Instron) connected to a digital multimeter (34465A, Keysight) for a real-time monitor of resistance change. A customized rigid acrylic cylindrical probe (10 mm diameter) was fixed in the upper gripper of testing machine, its flat end was pressed onto the samples with a sequential displacement increment of 0.01 mm s^{-1}. Furthermore, a parameter analyzer (4200-SCS, Keithley) was used to measure the *I*–*t* curves in the potential application of tactile-sensing. In the robot hand operation, an assembled programmable humanoid manipulator was employed. A standard SPS and a commercial flexible pressure sensor (FSR 400, Interlink Electronics) were successively attached to the middle finger of manipulator by a double sides adhesive tape. Both of sensors were operated under 0.3 V steady voltage.

Calculations: (1) Sensitivity (*S*)

$$S = \frac{\Delta I/I_0}{\Delta P} \text{ or } \frac{\Delta R/R_0}{\Delta P} \tag{1}$$

where I_0 (R_0) is the initial current (resistance) of SPS operated without pressure loading and ΔI (ΔR) is the current (resistance) change of the sensor under ΔP pressure loading.

(2) Gauge factor (GF)

$$\text{GF} = \frac{\Delta I/I_0}{\Delta L/L_0} = \frac{(I-I_0)/I_0}{\varepsilon} \text{ or } \frac{(R-R_0)/R_0}{\varepsilon} \tag{2}$$

where I (R) is measured current (resistance) at certain strain, I_0 (R_0) is the initial current (resistance), and ε is the strain.

(3) Temperature coefficient of resistance (TCR)

$$\text{TCR} = \frac{R-R_0}{R_0(T_R-T_0)} \tag{3}$$

where R is measured resistance at current temperature T_R, R_0, and T_0 are the initial resistance and temperature, respectively.

Supporting Information

Supporting Information is available from the Wiley Online Library or from the author.

Acknowledgements

This work was supported by the National Natural Science Foundation of China (61671308, U1613212), China Postdoctoral Science Foundation (2017M622774), Natural Science Foundation of Guangdong Province (2018A030310551, 2018A030310552), Department of Education of Guangdong Province (2016KZDXM005), and the Science and Technology Innovation Commission of Shenzhen (JCYJ20170818091233245). The authors thank Prof. Chaoyi Yan from Shenzhen University for helpful suggestions on the manuscript.

Conflict of Interest

The authors declare no conflict of interest.

Keywords

3D printing, hierarchical porosity, piezoresistive sensor, stretchable electronics

Received: October 26, 2018
Revised: December 3, 2018
Published online: December 27, 2018

[1] D. Son, J. Lee, S. Qiao, R. Ghaffari, J. Kim, J. E. Lee, C. Song, S. J. Kim, D. J. Lee, S. W. Jun, S. Yang, M. Park, J. Shin, K. Do, M. Lee, K. Kang, C. S. Hwang, N. Lu, T. Hyeon, D. H. Kim, *Nat. Nanotechnol.* **2014**, *9*, 397.

[2] J. W. Jeong, W. H. Yeo, A. Akhtar, J. J. Norton, Y. J. Kwack, S. Li, S. Y. Jung, Y. Su, W. Lee, J. Xia, H. Cheng, Y. Huang, W. S. Choi, T. Bretl, J. A. Rogers, *Adv. Mater.* **2013**, *25*, 6839.
[3] S. Wang, J. Xu, W. Wang, G. N. Wang, R. Rastak, F. Molinalopez, J. W. Chung, S. Niu, V. R. Feig, J. Lopez, T. Lei, S. K. Kwon, Y. Kim, A. M. Foudeh, A. Gasperini, Y. Yun, B. Murmann, J. B. Tok, Z. Bao, *Nature* **2018**, *555*, 7694.
[4] B. Gorissen, D. Reynaerts, S. Konishi, K. Yoshida, J. W. Kim, M. De Volder, *Adv. Mater.* **2017**, *29*, 1604977.
[5] M. Amjadi, K. U. Kyung, I. Park, M. Sitti, *Adv. Funct. Mater.* **2016**, *26*, 1678.
[6] J. T. Muth, D. M. Vogt, R. L. Truby, Y. Mengüç, D. B. Kolesky, R. J. Wood, J. A. Lewis, *Adv. Mater.* **2014**, *26*, 6307.
[7] C. Yan, J. Wang, W. Kang, M. Cui, X. Wang, C. Y. Foo, K. J. Chee, P. S. Lee, *Adv. Mater.* **2014**, *26*, 2022.
[8] J. Park, Y. Lee, J. Hong, M. Ha, Y. D. Jung, H. Lim, S. Y. Kim, H. Ko, *ACS Nano* **2014**, *8*, 4689.
[9] G. Schwartz, B. C. Tee, J. Mei, A. L. Appleton, D. H. Kim, H. Wang, Z. Bao, *Nat. Commun.* **2013**, *4*, 1859.
[10] T. Q. Trung, N. E. Lee, *Adv. Mater.* **2016**, *28*, 4338.
[11] S. C. B. Mannsfeld, B. C. Tee, R. M. Stoltenberg, C. V. H. Chen, S. Barman, B. V. O. Muir, A. N. Sokolov, C. Reese, Z. Bao, *Nat. Mater.* **2010**, *9*, 859.
[12] X. Wang, Y. Gu, Z. Xiong, Z. Cui, T. Zhang, *Adv. Mater.* **2014**, *26*, 1336.
[13] Y. Jiang, Z. Liu, N. Matsuhisa, D. Qi, W. R. Leow, H. Yang, J. Yu, G. Chen, Y. Liu, C. Wan, Z. Liu, X. Chen, *Adv. Mater.* **2018**, *30*, 1706589.
[14] A. Chortos, J. Liu, Z. Bao, *Nat. Mater.* **2016**, *15*, 937.
[15] J. Park, Y. Lee, J. Hong, Y. Lee, M. Ha, Y. Jung, H. Lim, S. Y. Kim, H. Ko, *ACS Nano* **2014**, *8*, 12020.
[16] S. Xu, Y. Zhang, L. Jia, K. E. Mathewson, K. I. Jang, J. Kim, H. Fu, X. Huang, P. Chava, R. Wang, S. Bhole, L. Wang, Y. J. Na, Y. Guan, M. Flavin, Z. Han, Y. Huang, J. A. Rogers, *Science* **2014**, *344*, 70.
[17] E. Roh, H. B. Lee, D. I. Kim, N. E. Lee, *Adv. Mater.* **2017**, *29*, 1703004.
[18] S. Jung, J. H. Kim, J. Kim, S. Choi, J. Lee, I. Park, T. Hyeon, D. H. Kim, *Adv. Mater.* **2014**, *26*, 4825.
[19] R. L. Truby, J. A. Lewis, *Nature* **2016**, *540*, 371.
[20] Y. Zhang, F. Zhang, Z. Yan, Q. Ma, X. Li, Y. Huang, J. A. Rogers, *Nat. Rev. Mater.* **2017**, *2*, 17019.
[21] S. Z. Guo, K. Qiu, F. Meng, S. H. Park, M. C. Mcalpine, *Adv. Mater.* **2017**, *29*, 1701218.
[22] Z. Lv, Y. Luo, Y. Tang, J. Wei, Z. Zhu, X. Zhou, W. Li, Y. Zeng, W. Zhang, Y. Zhang, D. Qi, S. Pan, X. J. Loh, X. Chen, *Adv. Mater.* **2018**, *30*, 1704531.
[23] H. Ota, S. Emaminejad, Y. Gao, A. Zhao, E. Wu, S. Challa, K. Chen, H. M. Fahad, A. K. Jha, D. Kiriya, W. Gao, H. Shiraki, K. Morioka, A. R. Ferguson, K. E. Healy, R. W. Davis, A. Javey, *Adv. Mater. Technol.* **2016**, *1*, 1600013.
[24] Z. F. Liu, S. Fang, F. A. Moura, J. N. Ding, N. Jiang, J. Di, M. Zhang, X. Lepró, D. S. Galvão, C. S. Haines, N. Y. Yuan, S. G. Yin, D. W. Lee, R. Wang, H. Y. Wang, W. Lv, C. Dong, R. C. Zhang, M. J. Chen, Q. Yin, Y. T. Chong, R. Zhang, X. Wang, M. D. Lima, R. Ovalle-Robles, D. Qian, H. Lu, R. H. Baughman, *Science* **2015**, *349*, 400.
[25] J. Kim, G. A. Salvatore, H. Araki, A. M. Chiarelli, Z. Xie, A. Banks, X. Sheng, Y. Liu, J. W. Lee, K. I. Jang, S. Y. Heo, K. Cho, H. Luo, B. Zimmerman, J. Kim, L. Yan, X. Feng, S. Xu, M. Fabiani, G. Gratton, Y. Huang, U. Paik, J. A. Rogers, *Sci. Adv.* **2016**, *2*, e1600418.
[26] A. D. Valentine, T. A. Busbee, J. W. Boley, J. R. Raney, A. Chortos, A. Kotikian, J. D. Berrigan, M. F. Durstock, J. A. Lewis, *Adv. Mater.* **2017**, *29*, 1703817.
[27] S. Roh, D. P. Parekh, B. Bharti, S. D. Stoyanov, O. D. Velev, *Adv. Mater.* **2017**, *29*, 1701554.
[28] N. Luo, Y. Huang, J. Liu, S. C. Chen, C. P. Wong, N. Zhao, *Adv. Mater.* **2017**, *29*, 1702675.
[29] T. Yamada, Y. Hayamizu, Y. Yamamoto, Y. Yomogida, A. Izadinajafabadi, D. N. Futaba, K. Hata, *Nat. Nanotechnol.* **2011**, *6*, 296.
[30] C. Yan, J. Wang, W. Kang, M. Cui, X. Wang, C. Y. Foo, K. J. Chee, P. S. Lee, *Adv. Mater.* **2014**, *26*, 1950.
[31] W. H. Yeo, Y. S. Kim, J. Lee, A. Ameen, L. Shi, M. Li, S. Wang, R. Ma, S. H. Jin, Z. Kang, Y. Huang, J. A. Rogers, *Adv. Mater.* **2013**, *25*, 2773.
[32] X. Wang, M. Que, M. Chen, X. Han, X. Li, C. Pan, Z. L. Wang, *Adv. Mater.* **2017**, *29*, 1605817.
[33] W. W. Nichols, *Am. J. Hypertens.* **2005**, *18*, 3.
[34] K. Y. Chun, Y. J. Son, E. S. Jeon, S. Lee, C. S. Han, *Adv. Mater.* **2018**, *30*, 1706299.
[35] O. T. Inan, M. Etemadi, R. M. Wiard, L. Giovangrandi, G. T. Kovacs, *Physiol. Meas.* **2009**, *30*, 169.